A Magnetic Equivalent Circuit Based Modeling Framework for Electric Motors Applied to a PMSM With Winding Short Circuit

Gabriel Forstner, *Student Member, IEEE*, Andreas Kugi, *Senior Member, IEEE*, and Wolfgang Kemmetmüller, *Member, IEEE*

***Abstract*—Accurate and real-time capable mathematical models are an essential prerequisite for the design of model-based controller and estimation strategies for electric motors. Magnetic equivalent circuit (MEC) models have proven to be an interesting alternative to classical inductor models that are typically utilized for the controller design. MEC models allow for a systematic inclusion of magnetic saturation and nonfundamental wave behavior of motors, while still having a manageable model complexity. The systematic derivation of the model equations can be rather involved, if in addition to the magnetic circuit of the motor also the electric interconnection is taken into account. For this reason, a modeling framework for electric motors based on MEC models including the electric interconnection is proposed. It makes use of network theory, which allows to systemize and automate major parts of the modeling task. The presented framework can be applied to a wide range of electromagnetic actuators. The feasibility of the proposed framework is demonstrated by the application to the modeling of a PMSM with (turn-to-turn) winding short circuit. A comparison with measurement results shows a high model accuracy of the resulting real-time capable model both for healthy and faulty conditions.**

***Index Terms*—Magnetic equivalent circuit (MEC), model calibration, permanent magnet synchronous motor (PMSM), winding short circuits.**

I. Introduction

PERMANENT magnet synchronous motors (PMSMs) are used in various industrial applications due to their high power density and efficiency. Their (optimal) control remains a challenge in particular when the PMSM is operated in ranges where nonlinear effects as magnetic saturation are relevant. Moreover, in many recent applications as, e.g., automotive steering systems, a fault tolerant operation is demanded, see, e.g., [1]–[3]. A turn-to-turn winding short circuit of the stator coils is one of the most common faults in applications with PMSMs. Such faults commonly result in a nonlinear and asymmetrical behavior of the motor. Moreover, higher harmonics within the electromagnetic quantities of the machine can occur and high currents may arise in the shorted coil. This can lead to local magnetic saturation of the machine, see, e.g., [4]–[12]. In these cases, analytical models, or dq0-models, which frequently rely on fundamental wave approximations and on a magnetic linear behavior of the motor, cannot describe the real PMSM behavior with high accuracy. Nevertheless, control and fault detection strategies are mostly based on such dq0-models, see, e.g., [11]–[17]. This, as a matter of fact, brings along that an optimal performance cannot be achieved for fault cases or in operating ranges with significant magnetic saturation.

A well established method to account for magnetic saturation, nonfundamental wave behavior and asymmetrical operation of a PMSM are finite element (FE) models. FE models contain detailed information about the magnetic field in the electric machine. They allow for an accurate consideration of complex geometries and saturation effects, see, e.g., [8], [18], [19]. Their relatively high complexity, however, results in a high computational effort, which makes FE models hardly suitable for the design of model based real-time fault detection or control algorithms.

Magnetic equivalent circuit (MEC) models provide a good compromise between model complexity and accuracy. Therefore, they are a good basis for fast dynamical simulations and the model-based design of control and fault detection strategies. It is easily possible to systematically include the nonlinear material behavior and inhomogeneous air gap geometries in MEC models, see, e.g., [20]–[23]. In the authors' previous works [22], [23], it was shown that the application of network theory allows for a systematic derivation of the model equations even for large MECs. All these works lack the systematic incorporation of the electric interconnection of the motor coils with each other and to other electric components (e.g., a cable or an inverter) into the MEC model.

Therefore, a novel modeling framework for real-time applications of (nonlinear) electromagnetic actuators, including both the magnetic and the electric circuit utilizing graph theory, is presented in this article. It will be shown that a systematic and accurate description of PMSMs under healthy and faulty conditions is possible. In particular, a (turn-to-turn) short circuit

Manuscript received August 3, 2019; revised October 31, 2019, December 19, 2019, and February 25, 2020; accepted March 27, 2020. Date of publication April 7, 2020; date of current version July 20, 2020. This work was supported by Robert Bosch GMBH (CR/AEE). Recommended for publication by Associate Editor D. G. Xu. *(Corresponding author: Gabriel Forstner.)*

Gabriel Forstner and Wolfgang Kemmetmüller are with the Automation and Control Institute, TU Wien, 1040 Vienna, Austria (e-mail: forstner@acin.tuwien.ac.at; kemmetmueller@acin.tuwien.ac.at).

Andreas Kugi is with the Automation and Control Institute, TU Wien, 1040 Vienna, Austria, and also with the Center for Vision, Automation and Control, Austrian Institute of Technology, 1210 Vienna, Austria (e-mail: kugi@acin.tuwien.ac.at).

Color versions of one or more of the figures in this article are available online at https://ieeexplore.ieee.org.

Digital Object Identifier 10.1109/TPEL.2020.2986042

between the windings of a stator coil of a PMSM can be considered in a straightforward way. The foundation of this approach is the application of network theory to both the MEC and the electric network (cf. [23]–[25]).

The model proposed in this article is intended to serve as a basis for the design of model-based control, observer, and fault detection strategies. For these tasks, an accurate description of the input-to-output behavior in the entire operating range is essential, while high accuracy of, e.g., the flux densities in the machine is of less importance.

This article is structured as follows. In Section II, a framework for the systematic modeling of nonlinear electromagnetic networks coupled with nonlinear electric networks is derived. The proposed framework is applied to the modeling of a three-phase PMSM with a short circuit between the windings of one stator coil in Section III. Section IV deals with the model calibration and the validation by measurement results. Finally, a short conclusion and an outlook on future research is given in Section V.

II. Modeling Framework for Electromagnetic Actuators

In this section, a framework for the systematic mathematical modeling of electromagnetic actuators is presented, which comprises two main parts.

1) MEC model: The magnetic part of the electromagnetic actuator is described by an MEC model that basically describes the magnetic flux and magneto motive forces (mmf) in the actuator. It contains mmf sources to represent the coils and permanent magnets. Magnetic permeances are used to describe the core and the air gap. The magnetically linear air gap permeances are in general (nonlinear) functions of the position of the moving parts of the electromagnetic actuator (e.g., the rotor in the case of an electric machine). The permeances of the core are nonlinear functions of the corresponding mmf to account for magnetic saturation.

2) Electric network: The electric interconnection of the coils of the electromagnetic actuator is described by an electric network. It consists of voltage and current sources, (nonlinear) electric resistors, (nonlinear) capacitors, and (nonlinear) inductors. In this electric network, the coils of the electromagnetic actuator are represented by magnetically coupled (nonlinear) inductors.

The MEC and the electric network are coupled by the coils of the electromagnetic actuator. This means that the electric currents of the coils define the mmf of the corresponding mmf sources in the MEC, while the fluxes of these mmf sources define the flux linkage of the corresponding inductors in the electric network. Starting from the equations of the MEC and the electric network, an overall mathematical model of the electromagnetic actuator is derived in the following sections.

A. MEC Model

The magnetic part of the electromagnetic actuator is modeled by an MEC, see, e.g., [20], [23], [26]. The topology of the MEC can be described via network theory by defining a tree, which connects all nodes of the network without forming any meshes, see, e.g., [24]. In general, the choice of the tree is arbitrary but all mmf sources must be placed in the tree. Given a suitable tree, the topology of the network (i.e., the interconnection of the network components) is described by the incidence matrix $\mathbf{D}^{\mathrm{T}} = [\mathbf{D}_c^{\mathrm{T}}, \mathbf{D}_m^{\mathrm{T}}, \mathbf{D}_g^{\mathrm{T}}]$. This matrix can be separated into a part $\mathbf{D}_c$ linking the coils in the tree with the cotree elements, a part $\mathbf{D}_m$ defining the interconnection of the tree magnets with the cotree elements and a part $\mathbf{D}_g$, which connects the tree permeances with the cotree elements. Following the ideas and steps described in [23], the MEC can be described by the set of (nonlinear) algebraic equations

$$\begin{bmatrix} \bar{\mathbf{D}}_c \boldsymbol{\mathcal{G}}_c \bar{\mathbf{D}}_c^{\mathrm{T}} & \bar{\mathbf{D}}_c \boldsymbol{\mathcal{G}}_c \mathbf{D}_g^{\mathrm{T}} \\ \mathbf{D}_g \boldsymbol{\mathcal{G}}_c \bar{\mathbf{D}}_c^{\mathrm{T}} & \boldsymbol{\mathcal{G}}_t + \mathbf{D}_g \boldsymbol{\mathcal{G}}_c \mathbf{D}_g^{\mathrm{T}} \end{bmatrix} \begin{bmatrix} \mathbf{i}_{\bar{L}} \\ \mathbf{u}_{tg} \end{bmatrix} = \begin{bmatrix} \boldsymbol{\psi}_{\bar{L}} \\ \mathbf{0} \end{bmatrix} - \begin{bmatrix} \bar{\mathbf{D}}_c \\ \mathbf{D}_g \end{bmatrix} \boldsymbol{\mathcal{G}}_c \mathbf{D}_m^{\mathrm{T}} \mathbf{u}_{tm}. \tag{1}$$

Therein, $\bar{\mathbf{D}}_c = \mathbf{N}_c \mathbf{D}_c$ with $\mathbf{N}_c = \mathrm{diag}[N_{c,1}, \ldots, N_{c,nc}]$ is used, where $N_{c,j}$ is the number of turns of a coil $j = 1, \ldots, n_c$. The nonlinear magnetic permeances within the tree and cotree are described by the diagonal matrices $\boldsymbol{\mathcal{G}}_t(\mathbf{u}_{tg}, \varphi)$ and $\boldsymbol{\mathcal{G}}_c(\mathbf{u}_c, \varphi)$, respectively. They are functions of the mmf $\mathbf{u}_{tg}$ of the tree permeances and the mmf $\mathbf{u}_c = -\mathbf{D}^{\mathrm{T}}[\mathbf{u}_{tc}^{\mathrm{T}}\ \mathbf{u}_{tm}^{\mathrm{T}}\ \mathbf{u}_{tg}^{\mathrm{T}}]^{\mathrm{T}}$ of the cotree permeances. Furthermore, they are nonlinear functions of the mechanical degrees of freedom, which is the rotor angle φ for the considered motor. The mmf of the coils $\mathbf{u}_{tc}$ are calculated from the coil currents $\mathbf{i}_{\bar{L}}$ by $\mathbf{u}_{tc} = \mathbf{N}_c \mathbf{i}_{\bar{L}}$, $\mathbf{u}_{tm}$ describes the equivalent mmf of the permanent magnets and $\boldsymbol{\psi}_{\bar{L}}$ are the flux linkages of the coils of the motor, see [23] for a detailed description. Finally, the electromagnetic torque τ of the electromagnetic actuator is given by

$$\tau = \frac{1}{2} \left(\mathbf{u}_{tg}^{\mathrm{T}} \frac{\partial \boldsymbol{\mathcal{G}}_t}{\partial \varphi} \mathbf{u}_{tg} + \mathbf{u}_c^{\mathrm{T}} \frac{\partial \boldsymbol{\mathcal{G}}_c}{\partial \varphi} \mathbf{u}_c \right). \tag{2}$$

B. Electric Network

The electric interconnection of the electromagnetic actuator's coils is represented by an electric network. It can comprise capacitors (index C), resistors (index R), voltage sources (index V), current sources (index I), and inductors. The inductors are divided into magnetically coupled inductors (index $\bar{L}$), which represent the actuator coils, and magnetically uncoupled inductors (index $\hat{L}$), which, e.g., represent the inductance of long electric cables or the inverter.

The topology of the electric network is again described via network theory by defining a suitable tree, see, e.g., [24], [25]. The choice of the tree is arbitrary, but all voltage sources must be included in the tree and all current sources must be placed in the cotree. The resulting circuit equations are given by

$$\mathbf{i}_t = \mathbf{E} \mathbf{i}_c \tag{3a}$$

$$\mathbf{v}_c = -\mathbf{E}^{\mathrm{T}} \mathbf{v}_t \tag{3b}$$

where $\mathbf{E}$ is the incidence matrix of the electric network. The currents and voltages of the tree elements are given by $\mathbf{i}_t$ and $\mathbf{v}_t$. Furthermore, $\mathbf{i}_c$ and $\mathbf{v}_c$ denote the currents and voltages of the cotree elements. A beneficial structure of the incidence matrix $\mathbf{E}$

is achieved when the maximum number of capacitors is placed in the tree and the maximum number of inductors is placed in the cotree (cf. [25]). In the case when a node is connected to inductors only, the maximum number of magnetically uncoupled inductors should be placed in the cotree. If the currents of the tree and cotree are arranged in the form

$$\mathbf{i}_t = \begin{bmatrix} \mathbf{i}_{tC}^{\mathrm{T}} & \mathbf{i}_{tV}^{\mathrm{T}} & \mathbf{i}_{tR}^{\mathrm{T}} & \mathbf{i}_{t\bar{L}}^{\mathrm{T}} & \mathbf{i}_{t\hat{L}}^{\mathrm{T}} \end{bmatrix}^{\mathrm{T}} \tag{4a}$$

$$\mathbf{i}_c = \begin{bmatrix} \mathbf{i}_{cC}^{\mathrm{T}} & \mathbf{i}_{cR}^{\mathrm{T}} & \mathbf{i}_{cI}^{\mathrm{T}} & \mathbf{i}_{c\bar{L}}^{\mathrm{T}} & \mathbf{i}_{c\hat{L}}^{\mathrm{T}} \end{bmatrix}^{\mathrm{T}} \tag{4b}$$

then the incidence matrix reads as [25]

$$\mathbf{E} = \begin{bmatrix} \mathbf{E}_{CC} & \mathbf{E}_{CR} & \mathbf{E}_{CI} & \mathbf{E}_{C\bar{L}} & \mathbf{E}_{C\hat{L}} \\ \mathbf{0} & \mathbf{E}_{VR} & \mathbf{E}_{VI} & \mathbf{E}_{V\bar{L}} & \mathbf{E}_{V\hat{L}} \\ \mathbf{0} & \mathbf{E}_{RR} & \mathbf{E}_{RI} & \mathbf{E}_{R\bar{L}} & \mathbf{E}_{R\hat{L}} \\ \mathbf{0} & \mathbf{0} & \mathbf{0} & \mathbf{E}_{\bar{L}\bar{L}} & \mathbf{E}_{\bar{L}\hat{L}} \\ \mathbf{0} & \mathbf{0} & \mathbf{0} & \mathbf{0} & \mathbf{E}_{\hat{L}\hat{L}} \end{bmatrix}. \tag{5}$$

The electric network model is completed by the balance and constitutive equations of the network elements, which are formulated in the following.

1) Capacitors: The electric charge Q of a capacitor is described by the nonlinear relation $Q = C(v)v$, where $C(v)$ defines the voltage-dependent capacitance and v is the electric voltage at the capacitor. Applying this constitutive equation to the capacitors of the electric network gives

$$\begin{bmatrix} \mathbf{Q}_{tC} \\ \mathbf{Q}_{cC} \end{bmatrix} = \begin{bmatrix} \mathbf{C}_{tC} & \mathbf{0} \\ \mathbf{0} & \mathbf{C}_{cC} \end{bmatrix} \begin{bmatrix} \mathbf{v}_{tC} \\ -\mathbf{E}_{CC}^{\mathrm{T}} \mathbf{v}_{tC} \end{bmatrix} \tag{6}$$

where $\mathbf{Q}_{tC}$ and $\mathbf{Q}_{cC}$ describe the electric charges of the capacitors in the tree and cotree, respectively. The electric charge is described by the balance of charge in the form

$$\frac{\mathrm{d}}{\mathrm{d}t}\mathbf{Q}_{tC} = \mathbf{E}_{CC}\mathbf{i}_{cC} + \mathbf{E}_{CR}\mathbf{i}_{cR} + \mathbf{E}_{CI}\mathbf{i}_{cI} + \mathbf{E}_{C\hat{L}}\mathbf{i}_{c\hat{L}} + \mathbf{E}_{C\bar{L}}\mathbf{i}_{c\bar{L}} \tag{7a}$$

$$\frac{\mathrm{d}}{\mathrm{d}t}\mathbf{Q}_{cC} = \mathbf{i}_{cC}. \tag{7b}$$

2) Resistors: The constitutive equations of the (nonlinear) resistors are written in the form

$$\begin{bmatrix} \mathbf{i}_{tR} \\ \mathbf{i}_{cR} \end{bmatrix} = \begin{bmatrix} \mathbf{G}_{tR} & \mathbf{0} \\ \mathbf{0} & \mathbf{G}_{cR} \end{bmatrix} \begin{bmatrix} \mathbf{v}_{tR} \\ \mathbf{v}_{cR} \end{bmatrix} \tag{8}$$

where $\mathbf{G}_{tR}(\mathbf{v}_{tR})$ and $\mathbf{G}_{cR}(\mathbf{v}_{cR})$ define the (voltage-dependent) conductances of the resistors within the tree and cotree, respectively. The currents $\mathbf{i}_{tR}$ can be expressed as $\mathbf{i}_{tR} = \mathbf{E}_{RR}\mathbf{i}_{cR} + \mathbf{E}_{RI}\mathbf{i}_{cI} + \mathbf{E}_{R\hat{L}}\mathbf{i}_{c\hat{L}} + \mathbf{E}_{R\bar{L}}\mathbf{i}_{c\bar{L}}$ according to (3)–(5). Furthermore, $\mathbf{v}_{cR} = -\mathbf{E}_{CR}^{\mathrm{T}}\mathbf{v}_{tC} - \mathbf{E}_{VR}^{\mathrm{T}}\mathbf{v}_{tV} - \mathbf{E}_{RR}^{\mathrm{T}}\mathbf{v}_{tR}$ holds. Utilizing these results yields the set of nonlinear algebraic equations

$$\begin{bmatrix} \mathbf{G}_{tR} & -\mathbf{E}_{RR}\mathbf{G}_{cR} \\ \mathbf{E}_{RR}^{\mathrm{T}} & \mathbf{I} \end{bmatrix} \begin{bmatrix} \mathbf{v}_{tR} \\ \mathbf{v}_{cR} \end{bmatrix} = \begin{bmatrix} \mathbf{E}_{RI}\mathbf{i}_{cI} + \mathbf{E}_{R\bar{L}}\mathbf{i}_{c\bar{L}} + \mathbf{E}_{R\hat{L}}\mathbf{i}_{c\hat{L}} \\ -\mathbf{E}_{CR}^{\mathrm{T}}\mathbf{v}_{tC} - \mathbf{E}_{VR}^{\mathrm{T}}\mathbf{v}_{tV} \end{bmatrix} \tag{9}$$

which has to be solved for $\mathbf{v}_{tR}$ and $\mathbf{v}_{cR}$, where $\mathbf{I}$ describes the identity matrix of suitable dimension.

3) Inductors: As mentioned before, the inductive circuit elements are divided into magnetically coupled and uncoupled inductors. The magnetically coupled inductors represent the magnetic part of the electromagnetic actuator (or other electromagnetically coupled inductors as, e.g., transformers), whose equations are given in Section II-A. The differential equations of the flux linkages are defined by Faraday's law of induction

$$\frac{\mathrm{d}}{\mathrm{d}t}\boldsymbol{\psi}_{t\bar{L}} = \mathbf{v}_{t\bar{L}} \tag{10a}$$

$$\frac{\mathrm{d}}{\mathrm{d}t}\boldsymbol{\psi}_{c\bar{L}} = -\mathbf{E}_{C\bar{L}}^{\mathrm{T}}\mathbf{v}_{tC} - \mathbf{E}_{V\bar{L}}^{\mathrm{T}}\mathbf{v}_{tV} - \mathbf{E}_{R\bar{L}}^{\mathrm{T}}\mathbf{v}_{tR} - \mathbf{E}_{\bar{L}\bar{L}}^{\mathrm{T}}\mathbf{v}_{t\bar{L}} \tag{10b}$$

where $\boldsymbol{\psi}_{t\bar{L}}$ and $\boldsymbol{\psi}_{c\bar{L}}$ are the flux linkages of the coils that are placed in the tree and cotree of the electric network, respectively. Note that by a suitable arrangement of the entries of $\boldsymbol{\psi}_{\bar{L}}$, $\boldsymbol{\psi}_{\bar{L}}^{\mathrm{T}} = [\boldsymbol{\psi}_{t\bar{L}}^{\mathrm{T}}, \boldsymbol{\psi}_{c\bar{L}}^{\mathrm{T}}]$, and $\mathbf{i}_{\bar{L}}^{\mathrm{T}} = [\mathbf{i}_{t\bar{L}}^{\mathrm{T}}, \mathbf{i}_{c\bar{L}}^{\mathrm{T}}]$ hold.

The magnetically uncoupled inductors are modeled by the nonlinear constitutive equations

$$\underbrace{\begin{bmatrix} \boldsymbol{\psi}_{t\hat{L}} \\ \boldsymbol{\psi}_{c\hat{L}} \end{bmatrix}}_{\boldsymbol{\psi}_{\hat{L}}} = \underbrace{\begin{bmatrix} \mathbf{L}_{t\hat{L}} & \mathbf{0} \\ \mathbf{0} & \mathbf{L}_{c\hat{L}} \end{bmatrix}}_{\mathbf{L}_{\hat{L}}} \underbrace{\begin{bmatrix} \mathbf{i}_{t\hat{L}} \\ \mathbf{i}_{c\hat{L}} \end{bmatrix}}_{\mathbf{i}_{\hat{L}}} \tag{11}$$

where the positive definite inductance matrix $\mathbf{L}_{\hat{L}}$ is in general a nonlinear function of the currents $\mathbf{i}_{t\hat{L}} = \mathbf{E}_{\hat{L}\hat{L}}\mathbf{i}_{c\hat{L}}$ and $\mathbf{i}_{c\hat{L}}$. The differential equations of the flux linkages $\boldsymbol{\psi}_{t\hat{L}}$ and $\boldsymbol{\psi}_{c\hat{L}}$ follow as

$$\frac{\mathrm{d}}{\mathrm{d}t}\boldsymbol{\psi}_{t\hat{L}} = \mathbf{v}_{t\hat{L}} \tag{12a}$$

$$\frac{\mathrm{d}}{\mathrm{d}t}\boldsymbol{\psi}_{c\hat{L}} = -\mathbf{E}_{C\hat{L}}^{\mathrm{T}}\mathbf{v}_{tC} - \mathbf{E}_{V\hat{L}}^{\mathrm{T}}\mathbf{v}_{tV} - \mathbf{E}_{R\hat{L}}^{\mathrm{T}}\mathbf{v}_{tR} - \mathbf{E}_{\hat{L}\hat{L}}^{\mathrm{T}}\mathbf{v}_{t\hat{L}} - \mathbf{E}_{\bar{L}\hat{L}}^{\mathrm{T}}\mathbf{v}_{t\bar{L}}. \tag{12b}$$

C. Elimination of Dependent Variables

The MEC model and the equations of the electric interconnection given in Sections II-A and II-B describe the overall behavior of the electromagnetic actuator. It, however, contains a number of dependent variables, whose elimination is meaningful, both for fast numeric simulations and for a model-based controller design. This section is, thus, concerned with the derivation of a mathematical model with a minimum number of state variables.

To do so, first the charges of the capacitors are considered. It is obvious that the voltage $\mathbf{v}_{tC}$ can be calculated as a function of the variable $\mathbf{Q}_{tC}$ by solving (6). This implies that the charge $\mathbf{Q}_{cC}$ is a dependent variable, since it can be expressed as $\mathbf{Q}_{cC} = -\mathbf{C}_{cC}\mathbf{E}_{CC}^{\mathrm{T}}\mathbf{v}_{tC}(\mathbf{Q}_{tC})$. To eliminate the unknown current $\mathbf{i}_{cC}$ from the set of equations, the new (independent) state $\mathbf{Q}_C^I = \mathbf{Q}_{tC} - \mathbf{E}_{CC}\mathbf{Q}_{cC}$ is introduced

$$\mathbf{Q}_C^I = \left[\mathbf{C}_{tC} + \mathbf{E}_{CC}\mathbf{C}_{cC}\mathbf{E}_{CC}^{\mathrm{T}}\right]\mathbf{v}_{tC}. \tag{13}$$

This independent state $\mathbf{Q}_C^I$ is described by the nonlinear differential equation

$$\frac{\mathrm{d}}{\mathrm{d}t}\mathbf{Q}_C^I = \mathbf{E}_{CR}\mathbf{i}_{cR} + \mathbf{E}_{CI}\mathbf{i}_{cI} + \mathbf{E}_{C\hat{L}}\mathbf{i}_{c\hat{L}} + \mathbf{E}_{C\bar{L}}\mathbf{i}_{c\bar{L}}. \tag{14}$$

The inductor currents are determined by the cotree currents $\mathbf{i}_{c\hat{L}}$ and $\mathbf{i}_{c\bar{L}}$ since

$$\begin{bmatrix}\mathbf{i}_{\hat{L}}\\ \mathbf{i}_{\bar{L}}\end{bmatrix} = \underbrace{\begin{bmatrix}\mathbf{E}_{\hat{L}\hat{L}} & \mathbf{0}\\ \mathbf{I} & \mathbf{0}\\ \mathbf{E}_{\bar{L}\hat{L}} & \mathbf{E}_{\bar{L}\bar{L}}\\ \mathbf{0} & \mathbf{I}\end{bmatrix}}_{\mathbf{V}_L^I} \underbrace{\begin{bmatrix}\mathbf{i}_{c\hat{L}}\\ \mathbf{i}_{c\bar{L}}\end{bmatrix}}_{\mathbf{i}_{cL}} = \begin{bmatrix}\mathbf{V}_{\hat{L}}^I\\ \mathbf{V}_{\bar{L}}^I\end{bmatrix}\mathbf{i}_{cL} \tag{15}$$

holds, cf. (3a). Utilizing this result in (1) and (11) gives

$$\begin{bmatrix}\mathbf{L}_{\hat{L}}\mathbf{V}_{\hat{L}}^I & \mathbf{0}\\ \bar{\mathbf{D}}_c\boldsymbol{\mathcal{G}}_c\bar{\mathbf{D}}_c^{\mathrm{T}}\mathbf{V}_{\bar{L}}^I & \bar{\mathbf{D}}_c\boldsymbol{\mathcal{G}}_c\mathbf{D}_g^{\mathrm{T}}\\ \mathbf{D}_g\boldsymbol{\mathcal{G}}_c\bar{\mathbf{D}}_c^{\mathrm{T}}\mathbf{V}_{\bar{L}}^I & \boldsymbol{\mathcal{G}}_t + \mathbf{D}_g\boldsymbol{\mathcal{G}}_c\mathbf{D}_g^{\mathrm{T}}\end{bmatrix}\begin{bmatrix}\mathbf{i}_{cL}\\ \mathbf{u}_{tg}\end{bmatrix} = \begin{bmatrix}\boldsymbol{\psi}_{\hat{L}}\\ \boldsymbol{\psi}_{\bar{L}}\\ \mathbf{0}\end{bmatrix} - \begin{bmatrix}\mathbf{0}\\ \bar{\mathbf{D}}_c\\ \mathbf{D}_g\end{bmatrix}\boldsymbol{\mathcal{G}}_c\mathbf{D}_m^{\mathrm{T}}\mathbf{u}_{tm}. \tag{16}$$

Additionally, (15) implies that not all flux linkages $\boldsymbol{\psi}_L^{\mathrm{T}} = [\boldsymbol{\psi}_{\hat{L}}^{\mathrm{T}}, \boldsymbol{\psi}_{\bar{L}}^{\mathrm{T}}]$ are independent variables, which is further confirmed by the fact that (16) has more equations than unknown variables $\mathbf{i}_{c\hat{L}}$, $\mathbf{i}_{c\bar{L}}$, $\mathbf{u}_{tg}$. To separate the dependent from the independent variables, the matrix $\mathbf{V}_L^{\perp}$

$$\mathbf{V}_L^{\perp} = \begin{bmatrix}\mathbf{V}_{\hat{L}}^{\perp}\\ \mathbf{V}_{\bar{L}}^{\perp}\end{bmatrix} = \begin{bmatrix}\mathbf{I} & \mathbf{0}\\ -\mathbf{E}_{\hat{L}\hat{L}}^{\mathrm{T}} & -\mathbf{E}_{\bar{L}\hat{L}}^{\mathrm{T}}\\ \mathbf{0} & \mathbf{I}\\ \mathbf{0} & -\mathbf{E}_{\bar{L}\bar{L}}^{\mathrm{T}}\end{bmatrix} \tag{17}$$

is introduced, where $(\mathbf{V}_L^{\perp})^{\mathrm{T}}\mathbf{V}_L^I = \mathbf{0}$ and $(\mathbf{V}_L^I)^{\mathrm{T}}\mathbf{V}_L^{\perp} = \mathbf{0}$ holds. This allows to define the transformation matrix $\mathbf{T}_e = \mathrm{diag}[\mathbf{T}_{eL}, \mathbf{I}]$ with

$$\mathbf{T}_{eL} = \begin{bmatrix}(\mathbf{V}_L^{\perp})^{\mathrm{T}}\\ (\mathbf{V}_L^I)^{\mathrm{T}}\end{bmatrix} = \begin{bmatrix}(\mathbf{V}_{\hat{L}}^{\perp})^{\mathrm{T}} & (\mathbf{V}_{\bar{L}}^{\perp})^{\mathrm{T}}\\ (\mathbf{V}_{\hat{L}}^I)^{\mathrm{T}} & (\mathbf{V}_{\bar{L}}^I)^{\mathrm{T}}\end{bmatrix}. \tag{18}$$

Utilizing this transformation the independent flux linkage $\boldsymbol{\psi}_L^I = (\mathbf{V}_L^I)^{\mathrm{T}}\boldsymbol{\psi}_L$ and the dependent flux linkages $\boldsymbol{\psi}_L^{\perp} = (\mathbf{V}_L^{\perp})^{\mathrm{T}}\boldsymbol{\psi}_L$ of the inductor elements are defined. The differential equations for the independent flux linkages $\boldsymbol{\psi}_{\hat{L}}^I = \mathbf{E}_{\hat{L}\hat{L}}^{\mathrm{T}}\boldsymbol{\psi}_{t\hat{L}} + \boldsymbol{\psi}_{c\hat{L}} + \mathbf{E}_{\bar{L}\hat{L}}^{\mathrm{T}}\boldsymbol{\psi}_{t\bar{L}}$ and $\boldsymbol{\psi}_{\bar{L}}^I = \mathbf{E}_{\bar{L}\bar{L}}^{\mathrm{T}}\boldsymbol{\psi}_{t\bar{L}} + \boldsymbol{\psi}_{c\bar{L}}$ read as

$$\frac{\mathrm{d}}{\mathrm{d}t}\begin{bmatrix}\boldsymbol{\psi}_{\hat{L}}^I\\ \boldsymbol{\psi}_{\bar{L}}^I\end{bmatrix} = \begin{bmatrix}-\mathbf{E}_{C\hat{L}}^{\mathrm{T}}\mathbf{v}_{tC} - \mathbf{E}_{V\hat{L}}^{\mathrm{T}}\mathbf{v}_{tV} - \mathbf{E}_{R\hat{L}}^{\mathrm{T}}\mathbf{v}_{tR}\\ -\mathbf{E}_{C\bar{L}}^{\mathrm{T}}\mathbf{v}_{tC} - \mathbf{E}_{V\bar{L}}^{\mathrm{T}}\mathbf{v}_{tV} - \mathbf{E}_{R\bar{L}}^{\mathrm{T}}\mathbf{v}_{tR}\end{bmatrix}. \tag{19}$$

Applying $\mathbf{T}_e$ to the set of algebraic equations (16) gives, after some calculations

$$\mathbf{K}_L\begin{bmatrix}\mathbf{i}_{c\hat{L}}\\ \mathbf{i}_{c\bar{L}}\\ \mathbf{u}_{tg}\end{bmatrix} = \begin{bmatrix}\boldsymbol{\psi}_{\hat{L}}^I\\ \boldsymbol{\psi}_{\bar{L}}^I\\ \mathbf{0}\end{bmatrix} - \begin{bmatrix}\hat{\mathbf{D}}_c\\ \tilde{\mathbf{D}}_c\\ \mathbf{D}_g\end{bmatrix}\boldsymbol{\mathcal{G}}_c\mathbf{D}_m^{\mathrm{T}}\mathbf{u}_{tm} \tag{20}$$

with

$$\mathbf{K}_L = \begin{bmatrix}\hat{\mathbf{L}} + \hat{\mathbf{D}}_c\boldsymbol{\mathcal{G}}_c\hat{\mathbf{D}}_c^{\mathrm{T}} & \hat{\mathbf{D}}_c\boldsymbol{\mathcal{G}}_c\tilde{\mathbf{D}}_c^{\mathrm{T}} & \hat{\mathbf{D}}_c\boldsymbol{\mathcal{G}}_c\mathbf{D}_g^{\mathrm{T}}\\ \tilde{\mathbf{D}}_c\boldsymbol{\mathcal{G}}_c\hat{\mathbf{D}}_c^{\mathrm{T}} & \tilde{\mathbf{D}}_c\boldsymbol{\mathcal{G}}_c\tilde{\mathbf{D}}_c^{\mathrm{T}} & \tilde{\mathbf{D}}_c\boldsymbol{\mathcal{G}}_c\mathbf{D}_g^{\mathrm{T}}\\ \mathbf{D}_g\boldsymbol{\mathcal{G}}_c\hat{\mathbf{D}}_c^{\mathrm{T}} & \mathbf{D}_g\boldsymbol{\mathcal{G}}_c\tilde{\mathbf{D}}_c^{\mathrm{T}} & \boldsymbol{\mathcal{G}}_t + \mathbf{D}_g\boldsymbol{\mathcal{G}}_c\mathbf{D}_g^{\mathrm{T}}\end{bmatrix}, \tag{21}$$

$\hat{\mathbf{L}} = \mathbf{E}_{\hat{L}\hat{L}}^{\mathrm{T}}\mathbf{L}_{t\hat{L}}\mathbf{E}_{\hat{L}\hat{L}} + \mathbf{L}_{c\hat{L}}$, $\tilde{\mathbf{D}}_c = [\mathbf{E}_{\bar{L}\bar{L}}^{\mathrm{T}}, \mathbf{I}]\bar{\mathbf{D}}_c$ and $\hat{\mathbf{D}}_c = [\mathbf{E}_{\bar{L}\hat{L}}^{\mathrm{T}}, \mathbf{0}]\bar{\mathbf{D}}_c$. Furthermore, the relation for the dependent flux linkages

$$\begin{aligned}\boldsymbol{\psi}_L^{\perp} = {} & \big((\mathbf{V}_{\hat{L}}^{\perp})^{\mathrm{T}}\mathbf{L}_{\hat{L}}\mathbf{V}_{\hat{L}}^I + (\mathbf{V}_{\bar{L}}^{\perp})^{\mathrm{T}}\bar{\mathbf{D}}_c\boldsymbol{\mathcal{G}}_c\bar{\mathbf{D}}_c^{\mathrm{T}}\mathbf{V}_{\bar{L}}^I\big)\,\mathbf{i}_{cL}\\ & + (\mathbf{V}_{\bar{L}}^{\perp})^{\mathrm{T}}\bar{\mathbf{D}}_c\boldsymbol{\mathcal{G}}_c\mathbf{D}_g^{\mathrm{T}}\mathbf{u}_{tg} + (\mathbf{V}_{\bar{L}}^{\perp})^{\mathrm{T}}\bar{\mathbf{D}}_c\boldsymbol{\mathcal{G}}_c\mathbf{D}_m^{\mathrm{T}}\mathbf{u}_{tm}\end{aligned} \tag{22}$$

can be obtained. Note that the dependent flux linkage $\boldsymbol{\psi}_L^{\perp}$ does not appear in the remaining set of equations (20) and, therefore, will not be considered in the subsequent derivations.

Summing up, the steps described so far allow to eliminate those parts of the variables which are dependent due to the interconnection of the electric components. In the next step, the question if the algebraic equations (20) have a unique solution will be discussed.

Remark 1: The existence and uniqueness of a solution of (20) is equivalent to proving that $\mathbf{K}_L$ is positive definite. To do so, note that $\boldsymbol{\mathcal{G}}_c$, $\boldsymbol{\mathcal{G}}_t$, and $\hat{\mathbf{L}}$ are positive definite matrices by construction. Then, it can be shown that $\mathbf{K}_L$ is positive definite if and only if $\tilde{\mathbf{D}}_c$ has full row rank, i.e., it comprises linearly independent rows. The proof of this statement is rather lengthy but straightforward and thus skipped in this article.

Let us now assume that $\tilde{\mathbf{D}}_c$ has dependent rows, which can arise due to the magnetic coupling of the coils within the MEC. Then, the nonsingular transformation matrix $\mathbf{T}_m = \mathrm{diag}[\mathbf{I}, \mathbf{T}_{m\bar{L}}, \mathbf{I}]$, with

$$\mathbf{T}_{m\bar{L}} = \begin{bmatrix}\mathbf{T}_{m\bar{L}}^{\perp}\\ \mathbf{T}_{m\bar{L}}^I\end{bmatrix} \tag{23}$$

can be defined. Therein, $\mathbf{T}_{m\bar{L}}^I$ spans the image of $\tilde{\mathbf{D}}_c^{\mathrm{T}}$ and $\mathbf{T}_{m\bar{L}}^{\perp}$ corresponds to the orthogonal space of $\mathbf{T}_{m\bar{L}}^I$, i.e., $\mathbf{T}_{m\bar{L}}^{\perp}\tilde{\mathbf{D}}_c = \mathbf{0}$ holds.

Remark 2: It is always possible to define the matrices $\mathbf{T}_{m\bar{L}}^{\perp}$, $\mathbf{T}_{m\bar{L}}^I$ in a way that the transformation matrix $\mathbf{T}_{m\bar{L}}$ is orthogonal, i.e., that $\mathbf{T}_{m\bar{L}}^{-1} = \mathbf{T}_{m\bar{L}}^{\mathrm{T}}$ holds.

This transformation matrix is now applied to (20) in the form

$$\begin{aligned}\underbrace{\mathbf{T}_m\mathbf{K}_L\mathbf{T}_m^{\mathrm{T}}}_{\mathbf{K}_L^I}\mathbf{T}_m\begin{bmatrix}\mathbf{i}_{c\hat{L}}\\ \mathbf{i}_{c\bar{L}}\\ \mathbf{u}_{tg}\end{bmatrix} = {} & \mathbf{T}_m\begin{bmatrix}\boldsymbol{\psi}_{\hat{L}}^I\\ \boldsymbol{\psi}_{\bar{L}}^I\\ \mathbf{0}\end{bmatrix}\\ & - \mathbf{T}_m\begin{bmatrix}\hat{\mathbf{D}}_c\\ \tilde{\mathbf{D}}_c\\ \mathbf{D}_g\end{bmatrix}\boldsymbol{\mathcal{G}}_c\mathbf{D}_m^{\mathrm{T}}\mathbf{u}_{tm}.\end{aligned} \tag{24}$$

Using the abbreviation $\mathbf{T}^{I}_{m\bar{L}}\tilde{\mathbf{D}}_c = \tilde{\mathbf{D}}^{I}_c$, the matrix $\mathbf{K}^{I}_{L}$ is given by

$$\mathbf{K}^{I}_{L} = \begin{bmatrix} \hat{\mathbf{L}} + \hat{\mathbf{D}}_c\mathcal{G}_c\hat{\mathbf{D}}_c^{\mathrm{T}} & \mathbf{0} & \hat{\mathbf{D}}_c\mathcal{G}_c(\tilde{\mathbf{D}}^{I}_c)^{\mathrm{T}} & \hat{\mathbf{D}}_c\mathcal{G}_c\mathbf{D}_g^{\mathrm{T}} \\ \mathbf{0} & \mathbf{0} & \mathbf{0} & \mathbf{0} \\ \tilde{\mathbf{D}}^{I}_c\mathcal{G}_c\hat{\mathbf{D}}_c^{\mathrm{T}} & \mathbf{0} & \tilde{\mathbf{D}}^{I}_c\mathcal{G}_c(\tilde{\mathbf{D}}^{I}_c)^{\mathrm{T}} & \tilde{\mathbf{D}}^{I}_c\mathcal{G}_c\mathbf{D}_g^{\mathrm{T}} \\ \mathbf{D}_g\mathcal{G}_c\hat{\mathbf{D}}_c^{\mathrm{T}} & \mathbf{0} & \mathbf{D}_g\mathcal{G}_c(\tilde{\mathbf{D}}^{I}_c)^{\mathrm{T}} & \mathcal{G}_t + \mathbf{D}_g\mathcal{G}_c\mathbf{D}_g^{\mathrm{T}} \end{bmatrix} \tag{25}$$

and the vector of unknown variables can be formulated as

$$\mathbf{T}_m \begin{bmatrix} \mathbf{i}_{c\hat{L}} \\ \mathbf{i}_{c\bar{L}} \\ \mathbf{u}_{tg} \end{bmatrix} = \begin{bmatrix} \mathbf{i}_{c\hat{L}} \\ \mathbf{T}^{\perp}_{m\bar{L}}\mathbf{i}_{c\bar{L}} \\ \mathbf{T}^{I}_{m\bar{L}}\mathbf{i}_{c\bar{L}} \\ \mathbf{u}_{tg} \end{bmatrix} = \begin{bmatrix} \mathbf{i}_{c\hat{L}} \\ \mathbf{i}^{\perp}_{c\bar{L}} \\ \mathbf{i}^{I}_{c\bar{L}} \\ \mathbf{u}_{tg} \end{bmatrix}. \tag{26}$$

Furthermore, the application of the transformation to the right-hand side of (24) yields

$$\mathbf{T}_m \begin{bmatrix} \boldsymbol{\psi}^{I}_{\hat{L}} \\ \boldsymbol{\psi}^{I}_{\bar{L}} \\ \mathbf{0} \end{bmatrix} = \begin{bmatrix} \boldsymbol{\psi}^{I}_{\hat{L}} \\ \mathbf{T}^{\perp}_{m\bar{L}}\boldsymbol{\psi}^{I}_{\bar{L}} \\ \mathbf{T}^{I}_{m\bar{L}}\boldsymbol{\psi}^{I}_{\bar{L}} \\ \mathbf{0} \end{bmatrix} = \begin{bmatrix} \boldsymbol{\psi}^{I}_{\hat{L}} \\ \boldsymbol{\psi}^{I\perp}_{\bar{L}} \\ \boldsymbol{\psi}^{II}_{\bar{L}} \\ \mathbf{0} \end{bmatrix} \tag{27}$$

and

$$\mathbf{T}_m \begin{bmatrix} \hat{\mathbf{D}}_c \\ \tilde{\mathbf{D}}_c \\ \mathbf{D}_g \end{bmatrix} \mathcal{G}_c\mathbf{D}_m^{\mathrm{T}}\mathbf{u}_{tm} = \begin{bmatrix} \hat{\mathbf{D}}_c \\ \mathbf{0} \\ \tilde{\mathbf{D}}^{I}_c \\ \mathbf{D}_g \end{bmatrix} \mathcal{G}_c\mathbf{D}_m^{\mathrm{T}}\mathbf{u}_{tm}. \tag{28}$$

It can be directly concluded that $\boldsymbol{\psi}^{I\perp}_{\bar{L}} = \mathbf{0}$ must hold and $\mathbf{i}^{\perp}_{c\bar{L}}$ no longer appears in these equations. With these results, a reduced set of algebraic equations is defined by

$$\mathbf{K}^{I}_{Lr} \begin{bmatrix} \mathbf{i}_{c\hat{L}} \\ \mathbf{i}^{I}_{c\bar{L}} \\ \mathbf{u}_{tg} \end{bmatrix} = \begin{bmatrix} \boldsymbol{\psi}^{I}_{\hat{L}} \\ \boldsymbol{\psi}^{II}_{\bar{L}} \\ \mathbf{0} \end{bmatrix} - \begin{bmatrix} \hat{\mathbf{D}}_c \\ \tilde{\mathbf{D}}^{I}_c \\ \mathbf{D}_g \end{bmatrix} \mathcal{G}_c\mathbf{D}_m^{\mathrm{T}}\mathbf{u}_{tm} \tag{29}$$

where $\mathbf{K}^{I}_{Lr}$ results from (25) by eliminating the zero rows and columns.

In the final step, the transformation is applied to the differential equations for the independent flux linkages (19). Obviously, the differential equations for $\boldsymbol{\psi}^{I}_{\hat{L}}$ remains unchanged and since $\boldsymbol{\psi}^{I\perp}_{\bar{L}} = \mathbf{T}^{\perp}_{m\bar{L}}\boldsymbol{\psi}^{I}_{\bar{L}} = \mathbf{0}$, the differential equation for $\boldsymbol{\psi}^{I}_{\bar{L}}$ is split up in an algebraic equation

$$\mathbf{0} = \mathbf{T}^{\perp}_{m\bar{L}}\left(-\mathbf{E}^{\mathrm{T}}_{C\bar{L}}\mathbf{v}_{tC} - \mathbf{E}^{\mathrm{T}}_{V\bar{L}}\mathbf{v}_{tV} - \mathbf{E}^{\mathrm{T}}_{R\bar{L}}\mathbf{v}_{tR}\right) \tag{30}$$

and a differential equation for $\boldsymbol{\psi}^{II}_{\bar{L}} = \mathbf{T}^{I}_{m\bar{L}}\boldsymbol{\psi}^{I}_{\bar{L}}$

$$\frac{\mathrm{d}}{\mathrm{d}t}\boldsymbol{\psi}^{II}_{\bar{L}} = \mathbf{T}^{I}_{m\bar{L}}\left(-\mathbf{E}^{\mathrm{T}}_{C\bar{L}}\mathbf{v}_{tC} - \mathbf{E}^{\mathrm{T}}_{V\bar{L}}\mathbf{v}_{tV} - \mathbf{E}^{\mathrm{T}}_{R\bar{L}}\mathbf{v}_{tR}\right). \tag{31}$$

In conclusion, the overall mathematical model of the electromagnetic actuator, including its electric interconnection is given by a system of differential algebraic equations (DAEs), with the differential equations (14) for $\mathbf{Q}^{I}_{c}$, (19) for $\boldsymbol{\psi}^{I}_{\hat{L}}$, and (31) for $\boldsymbol{\psi}^{II}_{\bar{L}}$. The algebraic equations are given by (9), (13), (22), $\boldsymbol{\psi}^{I\perp}_{c\bar{L}} = \mathbf{0}$, (29), and (30). Finally, the torque results from (2).

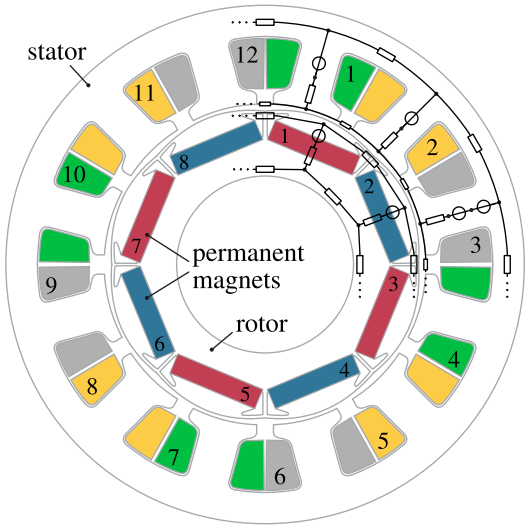

Fig. 1. Schematic of the considered three-phase PMSM.

Remark 3: The final DAE system is of index 1 and has a minimum number of states and algebraic variables. Its rather low numerical complexity allows for fast dynamic simulations and serves as a basis for the design of model-based control strategies, as, e.g., model-predictive control. If the magnetic saturation can be neglected and the electric components are linear, the resulting set of linear algebraic equations can be solved analytically, which results in a system of ordinary differential equations for the overall mathematical model of the electromagnetic actuator.

Remark 4: At a first glace, the proposed framework might seem to be rather complex due to the inherent reduction steps, which are based on linear algebra. It should, however, be noted that given an MEC and the electric network, all steps can be automated utilizing a computer algebra program. Currently, the authors are working on implementing the proposed modeling framework in a Maple package, which automatically derives all model equations and an (optimized) simulation code for MATLAB.

III. Model of a Three-Phase PMSM With Winding Short Circuit

In this section, the modeling framework described in the previous section is applied to systematically derive a mathematical model for a three-phase permanent magnet synchronous motor with a (turn-to-turn) winding short circuit of a stator coil. The considered PMSM comprises 12 single tooth coils, 8 internal permanent magnets, a skewed stator, and an inhomogeneous air gap (see Fig. 1). It is used in an automotive power steering application, where saturation of the stator may occur in typical operating scenarios. Safety is a very important feature for this type of application. Thus, it is required that typical fault cases, as the turn-to-turn winding short circuit, are taken into account in the design and operation of (model-based) control strategies. Therefore, a computationally efficient model that accurately covers also these fault cases is required.

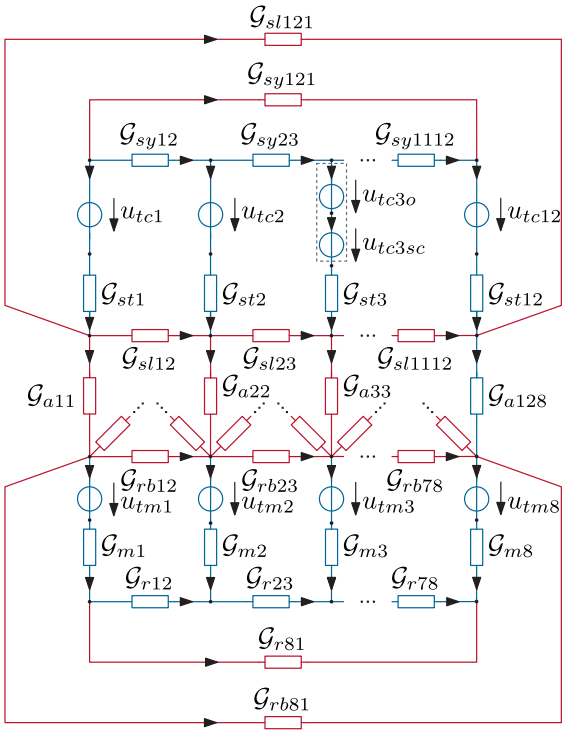

Fig. 2. Schematic of the MEC of the three-phase PMSM with a winding short circuit in coil 3. The tree of the network is indicated in blue with the corresponding cotree in red. The magnetic model of the turn-to-turn short circuit is highlighted by the dashed box.

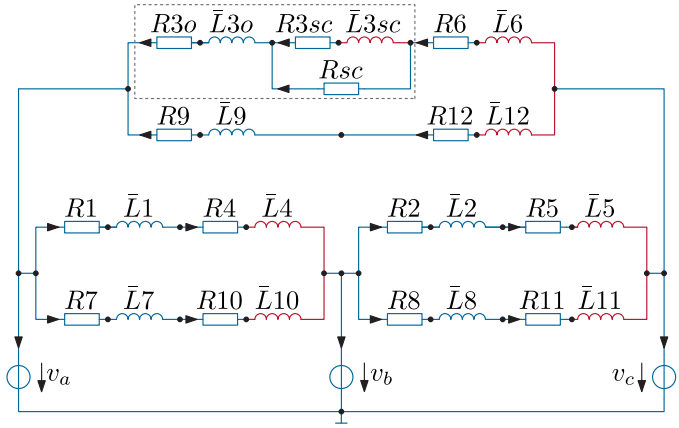

Fig. 3. Schematic of the electric interconnection of the three-phase PMSM with a winding short circuit in coil 3. The tree of the network is indicated in blue with the corresponding cotree in red. The electric model of the turn-to-turn short circuit is highlighted by the dashed box.

Following the procedure in Section II, first an MEC model is derived for the motor. The schematic of the MEC is depicted in Fig. 2. The main components are the mmf sources of the coils and the magnets, the nonlinear permeances of the stator and rotor, and the position-dependent air gap permeances. This choice of the MEC model is based on results known form the literature, in particular [20]–[23], [26]. In comparison to the models described in these references, an additional mmf source is utilized to model the turn-to-turn winding short circuit of the affected coil.

It is assumed that the short circuit affects coil 3. The turn-to-turn winding short circuit of this coil is modeled by splitting the coil into a part of N_{sc} shorted windings and $N_{\bar{L}} - N_{sc}$ windings of the healthy coil, where $N_{\bar{L}}$ is the number of windings of a stator coil. This is reflected in the MEC by two mmf sources u_{tc3o} and u_{tc3sc} in the stator tooth 3. The full range from a complete short circuit to a short circuit affecting one turn of coil 3 can be represented by changing the number N_{sc}. The remaining structure of the MEC is designed analogously to the MEC model proposed in [23], where also more details on the specific choice of the network can be found.

The electric interconnection of the coils is depicted in Fig. 3. In the considered system, the inverter is represented in an idealized form by the voltage sources v_a, v_b, and v_c. The coils are represented by the magnetically coupled inductors $\bar{L}$ and resistors R. Corresponding to the MEC, coil 3 is divided into the resistance R_{3o} and inductance $\bar{L}_{3o}$ of the healthy part, and R_{3sc} and $\bar{L}_{3sc}$ of the short circuited part. The resistance of the short circuit is described by R_{sc}. The tree in the schematic of the MEC in Fig. 2 and the electric interconnection in Fig. 3 is indicated in blue with the corresponding cotree in red.

The stator and rotor permeances of the motor can be directly modeled by design data of the machine and constitutive parameters of the material. Magnetic saturation of the stator and rotor is taken into account by nonlinear permeances $\boldsymbol{\mathcal{G}}_t$ and $\boldsymbol{\mathcal{G}}_c$, which are defined as functions of the corresponding mmfs. For instance a prismatic permeance of length l and area A can be written in the form $\mathcal{G} = \mu_0 \mu_r(u/l) A/l$, where u is the mmf at the permeance and $\mu_r(H) = \mu_r(u/l)$ is the nonlinear permeability function of the material [20], [23], [26].

The air gap permeances are modeled by

$$\mathcal{G}_a(\varphi) = \begin{cases} \mathcal{G}_{\bar{a}}(\varphi) & \text{for } -\pi/4 < \varphi < \pi/4 \\ 0 & \text{otherwise} \end{cases} \tag{32}$$

where the rotor angle φ is mapped to the interval $[-\pi, \pi]$ by means of a modulo operation and $\mathcal{G}_{\bar{a}}$ is defined by a Fourier series. The air gap permeances cannot be accurately described solely based on the geometry of the motor, since it is hardly possible to estimate the flux tube geometry of the air gap from the design data of the machine only. Thus, the coefficients of a Fourier series are identified based on measurements (or FE simulations) such that the input-to-output behavior of the model matches the measurements, see the discussion in Section IV. The air gap permeances are then defined by $\mathcal{G}_{ajk} = \mathcal{G}_a(\varphi - (j-1)\pi/6 - (k-1)\pi/4)$, with $j = 1, \ldots, 12$ and $k = 1, \ldots, 8$.

The currents of the voltage sources $\mathbf{i}_{tV}$, the resistive circuit elements $\mathbf{i}_{tR}$ and the magnetically coupled inductors $\mathbf{i}_{t\bar{L}}$ in the tree of the electric network are given by

$$\mathbf{i}_{tV} = [i_a \;\; i_b \;\; i_c]^{\mathrm{T}} \tag{33a}$$

$$\mathbf{i}_{tR} = [i_{R1} \; i_{R2} \;\; i_{R3o} \;\; i_{R3sc} \ldots i_{R12} \;\; i_{Rsc}]^{\mathrm{T}} \tag{33b}$$

$$\mathbf{i}_{t\bar{L}} = [i_{\bar{L}1} \;\; i_{\bar{L}2} \;\; i_{\bar{L}3o} \;\; i_{\bar{L}7} \;\; i_{\bar{L}8} \;\; i_{\bar{L}9}]^{\mathrm{T}}. \tag{33c}$$

The cotree comprises magnetically coupled inductors only, whose currents $\mathbf{i}_{c\bar{L}}$ are summarized as

$$\mathbf{i}_{c\bar{L}} = [i_{\bar{L}4} \;\; i_{\bar{L}5} \;\; i_{\bar{L}6} \;\; i_{\bar{L}10} \;\; i_{\bar{L}11} \;\; i_{\bar{L}12} \;\; i_{\bar{L}3\mathrm{sc}}]^{\mathrm{T}}. \tag{34}$$

The topology of the electric network can be formulated according to (3) and (5) by

$$\begin{bmatrix} \mathbf{i}_{tV} \\ \mathbf{i}_{tR} \\ \mathbf{i}_{t\bar{L}} \end{bmatrix} = \begin{bmatrix} \mathbf{E}_{V\bar{L}} \\ \mathbf{E}_{R\bar{L}} \\ \mathbf{E}_{\bar{L}\bar{L}} \end{bmatrix} \mathbf{i}_{c\bar{L}}. \tag{35}$$

After eliminating the dependent variables due to the electric interconnection, the MEC is described by

$$\mathbf{K}_L \begin{bmatrix} \mathbf{i}_{c\bar{L}} \\ \mathbf{u}_{tg} \end{bmatrix} = \begin{bmatrix} \boldsymbol{\psi}_{\bar{L}}^{I} \\ \mathbf{0} \end{bmatrix} - \begin{bmatrix} \tilde{\mathbf{D}}_c \\ \mathbf{D}_g \end{bmatrix} \boldsymbol{\mathcal{G}}_c \mathbf{D}_m^{\mathrm{T}} \mathbf{u}_{tm} \tag{36}$$

with

$$\mathbf{K}_L = \begin{bmatrix} \tilde{\mathbf{D}}_c \boldsymbol{\mathcal{G}}_c \tilde{\mathbf{D}}_c^{\mathrm{T}} & \tilde{\mathbf{D}}_c \boldsymbol{\mathcal{G}}_c \mathbf{D}_g^{\mathrm{T}} \\ \mathbf{D}_g \boldsymbol{\mathcal{G}}_c \tilde{\mathbf{D}}_c^{\mathrm{T}} & \boldsymbol{\mathcal{G}}_t + \mathbf{D}_g \boldsymbol{\mathcal{G}}_c \mathbf{D}_g^{\mathrm{T}} \end{bmatrix}. \tag{37}$$

The differential equation for the flux linkage reads as

$$\frac{\mathrm{d}}{\mathrm{d}t} \boldsymbol{\psi}_{\bar{L}}^{I} = -\mathbf{R}_{\bar{L}} \mathbf{i}_{c\bar{L}} - \mathbf{E}_{V\bar{L}}^{\mathrm{T}} \mathbf{v}_{tV}. \tag{38}$$

The assumed linear behavior of the resistors allows to solve $\mathbf{G}_{tR}\mathbf{v}_{tR} = \mathbf{E}_{R\bar{L}}\mathbf{i}_{c\bar{L}}$ for $\mathbf{v}_{tR}$. Using this result in (19) gives (38), where the abbreviation $\mathbf{R}_{\bar{L}} = \mathbf{E}_{R\bar{L}}^{\mathrm{T}} \mathbf{G}_{tR}^{-1} \mathbf{E}_{R\bar{L}}$ is introduced.

As discussed in Section II-C, the set of equations (36), (37) has to be further reduced, if $\tilde{\mathbf{D}}_c$ has linear dependent rows, which is the case for the considered system. Proceeding along the steps of Section II-C, the final model of the considered PMSM with (turn-to-turn) winding short circuit is given by

$$\frac{\mathrm{d}}{\mathrm{d}t} \boldsymbol{\psi}_{\bar{L}}^{II} = -\tilde{\mathbf{R}}_{\bar{L}} \mathbf{i}_{c\bar{L}}^{I} - \tilde{\mathbf{E}}_{V\bar{L}}^{\mathrm{T}} \mathbf{v}_{tV} \tag{39a}$$

$$\mathbf{K}_{Lr}^{I} \begin{bmatrix} \mathbf{i}_{c\bar{L}}^{I} \\ \mathbf{u}_{tg} \end{bmatrix} = \begin{bmatrix} \boldsymbol{\psi}_{\bar{L}}^{II} \\ \mathbf{0} \end{bmatrix} - \begin{bmatrix} \tilde{\mathbf{D}}_c^{I} \\ \mathbf{D}_g \end{bmatrix} \boldsymbol{\mathcal{G}}_c \mathbf{D}_m^{\mathrm{T}} \mathbf{u}_{tm} \tag{39b}$$

$$\tau = \frac{1}{2} \left(\mathbf{u}_{tg}^{\mathrm{T}} \frac{\partial \boldsymbol{\mathcal{G}}_t}{\partial \varphi} \mathbf{u}_{tg} + \mathbf{u}_c^{\mathrm{T}} \frac{\partial \boldsymbol{\mathcal{G}}_c}{\partial \varphi} \mathbf{u}_c \right). \tag{39c}$$

Here, the abbreviations

$$\tilde{\mathbf{R}}_{\bar{L}} = \mathbf{T}_{m\bar{L}}^{I} \Big(\mathbf{R}_{\bar{L}} - \mathbf{R}_{\bar{L}} (\mathbf{T}_{m\bar{L}}^{\perp})^{\mathrm{T}} \left(\mathbf{T}_{m\bar{L}}^{\perp} \mathbf{R}_{\bar{L}} (\mathbf{T}_{m\bar{L}}^{\perp})^{\mathrm{T}} \right)^{-1} \mathbf{T}_{m\bar{L}}^{\perp} \mathbf{R}_{\bar{L}} \Big) (\mathbf{T}_{m\bar{L}}^{I})^{\mathrm{T}} \tag{40}$$

and $\tilde{\mathbf{E}}_{V\bar{L}}^{\mathrm{T}} = \mathbf{T}_{m\bar{L}}^{I} \mathbf{E}_{V\bar{L}}^{\mathrm{T}}$ are used. This final DAE has six states $\boldsymbol{\psi}_{\bar{L}}^{II}$ and 45 algebraic variables $\mathbf{i}_{c\bar{L}}^{I}$, $\mathbf{u}_{tg}$.

IV. Model Calibration and Validation

Most of the model parameters of the proposed MEC can be accurately determined based on the geometric data of the motor and the material data of the core and the permanent magnets. In contrast, the value and shape of the air gap permeances $\mathcal{G}_a(\varphi)$ and the stator leakage permeances $\mathcal{G}_{sl}$ cannot be accurately determined by construction data only, since it is difficult to estimate the leakage flux paths. These permeances, however, strongly influence the behavior of the motor, in particular the torque. Thus, a calibration based on FE simulations or measurements is required for a high model accuracy.

In the following, a model calibration strategy for the proposed MEC model is described. Afterward, the accuracy of the calibrated model is demonstrated for a number of typical operating points of the PMSM, which cover both the nominal operation and the case of a winding short circuit.

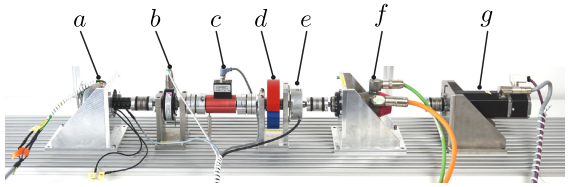

Fig. 4. Setup of the test stand: a PMSM under consideration, b rotary encoder, c torque sensor, d fly wheel, e rotary encoder, f harmonic drive, g load motor.

TABLE I
Components of the Test Stand and Measurement Setup

Description	Device
Measurement platform	dSpace MicroLab Box 1202
Current sensor	Sensitec CMS30050ABA
Voltage sensor	Knick P27000 H1
a test motor	PMSM under consideration
b rotary encoder	w+s IH951
c torque sensor	KTR Dataflex 16/10
d fly wheel	Inertia $J = 0.01\,\mathrm{kg\,m^2}$
e rotary encoder	Heidenhain ERN1205000
f load motor	Harmonic Drive LynxDrive-20C
g load motor	Dunker Motor BG75

A. Model Calibration

The model calibration described in this part is based on measurements of the PMSM on a test stand depicted in Fig. 4. Starting from the left, the test stand comprises the modeled PMSM, which is coupled to a rotary encoder, followed by a torque sensor, a fly wheel, a second rotary encoder, and a load machine. Depending on the experiment, the PMSM is either rotated at slow speed by a harmonic drive or driven at a higher speed by a load motor. The main components of the test stand and measurement setup are summarized in Table I.

The identification of the model parameters (i.e., the air gap permeances $\mathcal{G}_a(\varphi)$ and the stator leakage permeances $\mathcal{G}_{sl}$) is done for the healthy PMSM without a short circuit ($N_{sc} = 0$). This is reasonable, since the exact location and the number of shorted windings N_{sc} will not be available in practical applications and, thus, would also not be feasible for a model calibration.

The model calibration is based on the following measurements.

1) In the first experiment, the PMSM is rotated at a very slow speed of 1 r/min by the harmonic drive. Constant terminal currents $i_a = i_n$, $i_b = -i_n$, and $i_c = 0$ are applied, where i_n is the nominal current of the PMSM. The resulting torque τ is measured in one electric period

of $\varphi = 0, \ldots, 90^\circ$ with a step size of 0.5°. This results in $N^\tau = 180$ measurements of the torque τ_k^m, the angle φ_k^m, and the terminal currents $\mathbf{i}_{tV,k}^m = [i_{a,k}^m, i_{b,k}^m, i_{c,k}^m]^{\mathrm{T}}$, $k = 1, \ldots, N^\tau$.

2) In addition to the torque, the flux linkage $\boldsymbol{\psi}_{\bar{L}}^{II}$ is an important quantity for the model calibration. A direct measurement of the flux linkage is, as a matter of fact, typically not possible in a PMSM. Instead, measurements of the back emf of the motor for open terminals (terminal currents $i_a = i_b = i_c = 0$) are performed at a constant speed $n = 500$ r/min. Using $\mathbf{i}_{c\bar{L}}^I = \mathbf{0}$ and $\boldsymbol{\psi}_{\bar{L}}^{II}(\varphi, \mathbf{i}_{c\bar{L}}^I) = \boldsymbol{\psi}_{\bar{L}}^{II}(\varphi, \mathbf{0})$ in (39a) gives

$$\boldsymbol{\psi}_{\bar{L}}^{II}(\varphi, \mathbf{0}) - \boldsymbol{\psi}_{\bar{L}}^{II}(\varphi_0, \mathbf{0}) = -\frac{1}{\omega} \int_{\varphi_0}^{\varphi} \tilde{\mathbf{E}}_{V\bar{L}}^{\mathrm{T}} \mathbf{v}_{tV}^m \mathrm{d}\tilde{\varphi}. \quad (41)$$

The symmetry of the motor implies $\boldsymbol{\psi}_{\bar{L}}^{II}(\varphi, \mathbf{0}) = -\boldsymbol{\psi}_{\bar{L}}^{II}(\varphi + \pi/4, \mathbf{0})$, which allows to eliminate $\boldsymbol{\psi}_{\bar{L}}^{II}(\varphi_0, \mathbf{0})$ in (41). Then, the flux linkage for zero currents can be calculated in the form

$$\boldsymbol{\psi}_{\bar{L}}^{II}(\varphi, \mathbf{0}) = \frac{1}{2\omega} \int_{\varphi}^{\varphi+\pi/4} \tilde{\mathbf{E}}_{V\bar{L}}^{\mathrm{T}} \mathbf{v}_{tV}^m \mathrm{d}\tilde{\varphi}. \quad (42)$$

The flux linkage $\boldsymbol{\psi}_{\bar{L}}^{II}(\varphi, \mathbf{0}) = \boldsymbol{\psi}_{pm}^{II}(\varphi)$ is determined for a step size of 2°, which gives $N_\varphi^\psi = 45$ flux linkage values $\boldsymbol{\psi}_{pm,j}^{II,m}$ at the angles $\varphi_j^m = j\pi/90$, $j = 1, \ldots, N_\varphi^\psi$.

3) To obtain measurements of the flux linkage for nonzero currents, sinusoidal terminal currents $\mathbf{i}_{tV}$ with a constant time period $T^\psi = 2.5$ ms and amplitude i^ψ, which is approximately 75% of the maximum current of the PMSM, are applied by a simple current controller for fixed rotor angles $\varphi_j = j\pi/90$, $j = 1, \ldots, N_\varphi^\psi$. According to (39a), the flux linkage can be calculated by

$$\boldsymbol{\psi}_{\bar{L}}^{II}(\varphi_j, \mathbf{i}_{c\bar{L}}^I(t)) = \boldsymbol{\psi}_{pm,j}^{II} - \int_0^t \left(\tilde{\mathbf{R}}_{\bar{L}} \mathbf{i}_{c\bar{L}}^{I,m} + \tilde{\mathbf{E}}_{V\bar{L}}^{\mathrm{T}} \mathbf{v}_{tV}^m \right) \mathrm{d}\tilde{t}. \quad (43)$$

This integral is evaluated for $N_i^\psi = 9$ points with $t = t_l$ for each angle φ_j^m. This gives the flux linkage $\boldsymbol{\psi}_{\bar{L}}^{II,m}(\varphi_j^m, \mathbf{i}_{c\bar{L}}^{I,m}(t_l)) = \boldsymbol{\psi}_{\bar{L},jl}^{II,m}$ with the corresponding rotor angle φ_j^m, $j = 1, \ldots, N_\varphi^\psi$ and currents $\mathbf{i}_{c\bar{L},l}^{I,m}$, $l = 1, \ldots, N_i^\psi$.

Remark 5: The integration in (41) and (43) will have a drift if nonzero mean measurement errors are present in the voltage or current measurements. This drift, however, can be easily compensated by exploiting the fact that $\boldsymbol{\psi}_{\bar{L}}^{II}(\varphi_k, \mathbf{i}_{c\bar{L}}^I(t)) = \boldsymbol{\psi}_{\bar{L}}^{II}(\varphi_k, \mathbf{i}_{c\bar{L}}^I(t + T^\psi))$ and $\boldsymbol{\psi}_{\bar{L}}^{II}(\varphi_k, \mathbf{i}_{c\bar{L}}^I(t)) = \boldsymbol{\psi}_{\bar{L}}^{II}(\varphi_k + \pi/2, \mathbf{i}_{c\bar{L}}^I(t))$ hold for the motor without winding short circuits.

Based on these measurements, the air gap permeances $\mathcal{G}_a$ and the stator leakage permeances $\mathcal{G}_{sl}$ can be calibrated. As briefly discussed before, the shape of the air gap permeance is given by (32). A Fourier series of order N_a is utilized to approximate $\mathcal{G}_{\bar{a}}$, i.e.,

$$\mathcal{G}_{\bar{a}}(\varphi) = \alpha_0 + \sum_{n=1}^{N_a} \alpha_n \cos(np\varphi) + \beta_n \sin(np\varphi) \quad (44)$$

where $p = 4$ is the number of pole pairs of the PMSM. For the stator leakage permeances a nominal value can be approximated from geometry data in the form $\mathcal{G}_{sl}^{nom} = A_{sl}\mu_0/l_{sl}$, where A_{sl} defines the area and l_{sl} defines the length of the initial stator leakage permeance. It is assumed that the real stator leakage permeance is given by $\mathcal{G}_{sl} = \gamma \mathcal{G}_{sl}^{nom}$, with a scalar scaling parameter γ. This results in the parameters $\boldsymbol{\alpha} = [\alpha_0, \ldots, \alpha_{N_a}]^{\mathrm{T}}$, $\boldsymbol{\beta} = [\beta_1, \ldots, \beta_{N_a}]^{\mathrm{T}}$, and γ, which have to be identified.

The parameter calibration problem is formulated as a constrained optimization problem. The cost function $J = J^\tau + J^\psi$ to be minimized comprises a part J^τ, which penalizes the torque error

$$J^\tau = q_\tau \sum_{k=1}^{N^\tau} \left(\tau(\varphi_k^m, \mathbf{i}_{c\bar{L},k}^{I,m}, \mathbf{u}_{tg,k}) - \tau_k^m \right)^2 \quad (45)$$

where $q_\tau > 0$ is a scalar weighting parameter, and $\mathbf{u}_{tg,k}$ is defined by (39b), see (25), in the form

$$\begin{aligned} \mathbf{g}_k^\tau = & \left(\boldsymbol{\mathcal{G}}_t(\varphi_k^m) + \mathbf{D}_g \boldsymbol{\mathcal{G}}_c(\varphi_k^m) \mathbf{D}_g^{\mathrm{T}} \right) \mathbf{u}_{tg,k} \\ & + \mathbf{D}_g \boldsymbol{\mathcal{G}}_c(\varphi_k^m)((\tilde{\mathbf{D}}_c^I)^{\mathrm{T}} \mathbf{i}_{c\bar{L},k}^{I,m} + \mathbf{D}_m^{\mathrm{T}} \mathbf{u}_{tm}) = \mathbf{0}. \end{aligned} \quad (46)$$

The second part J^ψ of the cost function J is used to penalize errors in the flux linkage in the form

$$J^\psi = q_\psi \sum_{j=1}^{N_\varphi^\psi} \sum_{l=1}^{N_i^\psi} \left(\boldsymbol{\psi}_{\bar{L}}^{II}(\varphi_j^m, \mathbf{i}_{c\bar{L},l}^{I,m}) - \boldsymbol{\psi}_{\bar{L},jl}^{II,m} \right)^2 \quad (47)$$

with $q_\psi > 0$. The mmf $\mathbf{u}_{tg,lj}$ is defined similar to (46) by

$$\begin{aligned} \mathbf{g}_{lj}^\psi = & (\boldsymbol{\mathcal{G}}_t(\varphi_j^m) + \mathbf{D}_g \boldsymbol{\mathcal{G}}_c(\varphi_j^m) \mathbf{D}_g^{\mathrm{T}}) \mathbf{u}_{tg,lj} \\ & + \mathbf{D}_g \boldsymbol{\mathcal{G}}_c(\varphi_j^m)((\tilde{\mathbf{D}}_c^I)^{\mathrm{T}} \mathbf{i}_{c\bar{L},l}^{I,m} + \mathbf{D}_m^{\mathrm{T}} \mathbf{u}_{tm}) = \mathbf{0}. \end{aligned} \quad (48)$$

Furthermore, the torque $\tau(\varphi_k^m, \mathbf{i}_{c\bar{L},k}^{I,m}, \mathbf{u}_{tg,k})$ and the flux linkage $\boldsymbol{\psi}_{\bar{L}}^{II}(\varphi_j^m, \mathbf{i}_{c\bar{L},l}^{I,m})$ are defined by (39b) and (39c), respectively.

With these prerequisites, a constrained parameter optimization problem can be formulated as

$$\min_{\mathbf{X}} J \quad (49a)$$

s.t.

$$\mathbf{0} = \mathbf{g}_k^\tau, \quad k = 1, \ldots, N^\tau \quad (49b)$$

$$\mathbf{0} = \mathbf{g}_{lj}^\psi, \quad j = 1, \ldots, N_\varphi^\psi, l = 1, \ldots, N_i^\psi \quad (49c)$$

where

$$\mathbf{X} = \left\{ \boldsymbol{\alpha}, \boldsymbol{\beta}, \gamma, \mathbf{u}_{tg,1}, \ldots, \mathbf{u}_{tg,N^\tau}, \mathbf{u}_{tg,11}, \ldots, \mathbf{u}_{tg,N_\varphi^\psi N_i^\psi} \right\} \quad (50)$$

summarizes all optimization variables. This rather large constrained optimization problem is solved by applying the reduced gradient method, see, e.g., [27], [28]. The main idea is to split the optimization variables into a set $\mathbf{X}_d$ of optimization variables that are fixed by the equality constraints and a set $\mathbf{X}_i$ of independent optimization variables. This allows to partially decouple the solution of the nonlinear equality constraints from the optimization. The mmf $\mathbf{u}_{tg}$ are chosen as dependent variables, which leaves the unknown system parameters $\boldsymbol{\alpha}$, $\boldsymbol{\beta}$, and γ as the independent optimization variables. The resulting optimization

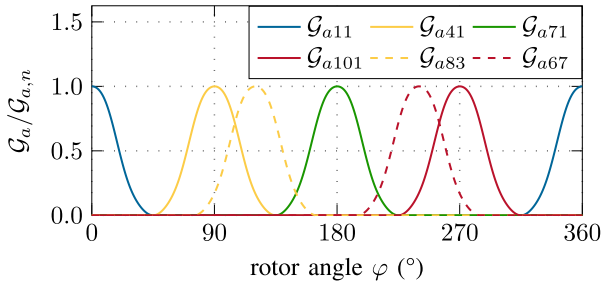

Fig. 5. Shape of the optimal air gap permeances $\mathcal{G}_{ajk}(\varphi)$ between individual coils j and magnets k.

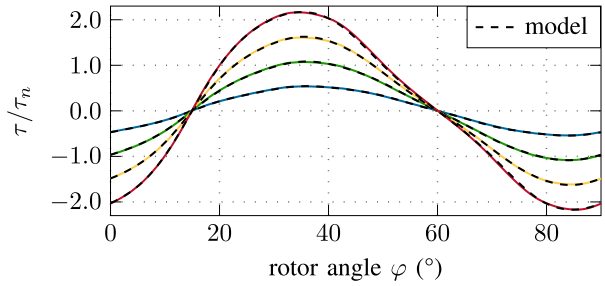

Fig. 6. Validation of the calibrated model for the nominal healthy case: torque τ for terminal currents $i_a = i_p$, $i_b = -i_p$ and $i_c = 0$, with i_p ranging from $i_n/2$ to $2i_n$.

problem is iteratively solved in MATLAB. The solution time of the optimization problem is in the range of 15 min on a PC with Intel Core I7 processor.

The resulting optimal shape of the air gap permeances $\mathcal{G}_a(\varphi)$ is depicted in Fig. 5. It constitutes a smooth and symmetric function with a distinct fundamental wave, which agrees with the skewed stator of the considered PMSM. Furthermore, the optimal scaling factor of the stator leakage permeance results in $\gamma = 3.7$, which implies that the nominal stator leakage permeance was assumed too small.

B. Model Validation

In this section, the accuracy of the calibrated model is evaluated by comparison with measurement results, both for the nominal case and the case of a winding short circuit. As mentioned before, the parameter identification was performed for the healthy PMSM without a short circuit. Thus, in the first step the model accuracy for the nominal case of a healthy PMSM is evaluated.

Fig. 6 shows the comparison of the torque τ of the calibrated model with measurements for terminal currents $i_a = i_p$, $i_b = -i_p$, and $i_c = 0$, where i_p ranges from $i_n/2$ to $2i_n$. These results show that the proposed MEC model exhibits an excellent accuracy of the torque in the entire feasible operating range of the PMSM. It should be noted that only measurements at $i_p = i_n$ were used for the model calibration. A closer look at the results in Fig. 6 reveals that the shape of the torque has nonvanishing higher harmonics, which become more pronounced for higher currents. This can be attributed to the magnetic saturation of the motor, which becomes larger for higher currents. The results

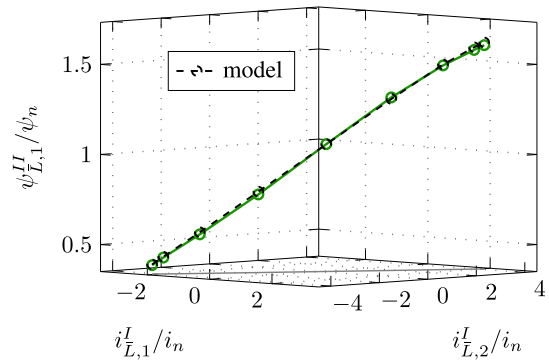

Fig. 7. Validation of the calibrated model for the nominal healthy case: flux linkage $\psi^I_{\bar{L},1}$ for a constant angle $\varphi = 45°$.

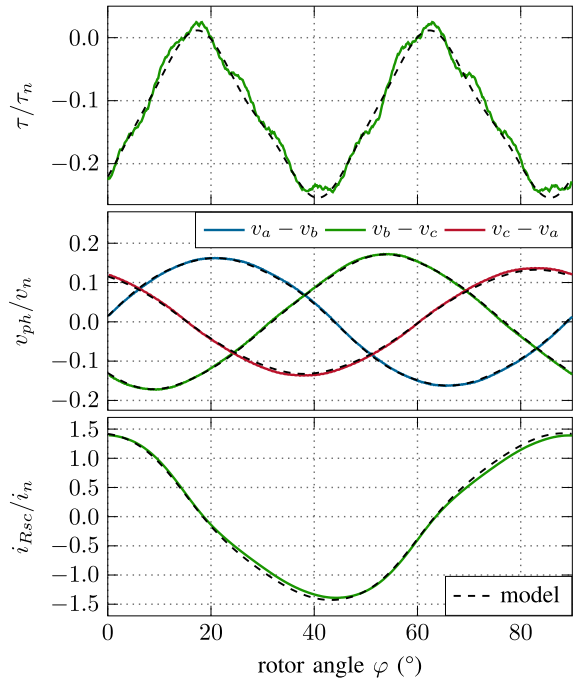

Fig. 8. Validation of the calibrated model for a winding short circuit in coil 3 at a rotational speed of $n = 300$ r/min and open terminals: torque τ, phase voltages v_{ph} between the terminals, and current i_{Rsc} in the short-circuit path.

depicted in Fig. 6, thus, also show that magnetic saturation is accurately covered by the proposed model.

The second evaluation of the model is based on the reduced flux linkages $\boldsymbol{\psi}^{II}_{\bar{L}}$. Fig. 7 gives a comparison of the flux linkage of the model with the flux linkage calculated from current and voltage measurements according to the description given in the previous section. It can be observed that again a good matching of the model is achieved for the entire operating range. Please note that the bend in the curve in Fig. 7 for high values of $i^I_{\bar{L},1}$ and $i^I_{\bar{L},2}$ can again be attributed to magnetic saturation. This effect is also accurately captured by the proposed model.

In the next step, the accuracy of the proposed model for a complete winding short circuit of coil 3 ($N_{\mathrm{sc}} = N_{\bar{L}}$) is investigated. The PMSM is rotated at a constant speed of $n = 300$ r/min and open terminals are considered in the first experiment. Fig. 8 depicts the results for the torque τ, the voltages between

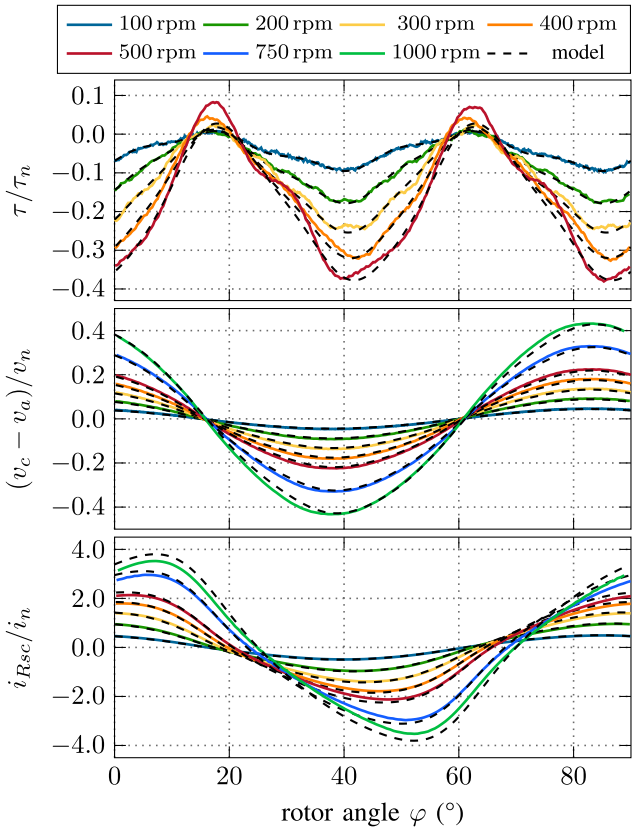

Fig. 9. Validation of the calibrated model for a winding short circuit in coil 3 at different rotational speeds from $n = 100$ r/min to $n = 1000$ r/min and open terminals: torque τ, voltage $v_c - v_a$, and current i_{Rsc} in the short circuit path. The rated speed of the considered motor is given by 1300 r/min.

the terminals $v_a - v_b$, $v_b - v_c$, $v_c - v_a$, and the current i_{Rsc} in the short circuit path. These results confirm that the proposed model is able to accurately describe the relevant system variables also in the case of a winding short circuit. In particular, a good agreement of the resulting short-circuit current i_{Rsc} and of the back emf at the terminals can be seen. The basic shape of the torque is also well described by the proposed model. The higher harmonics within the torque measurements can be partially related to mechanical vibrations on the test stand.

Finally, Fig. 9 shows results of the PMSM with winding short circuit of coil 3 ($N_{sc} = N_{\bar{L}}$) for different values of the rotational speed n. Again, a good accuracy of the proposed model is achieved, in particular for the voltage $v_c - v_a$ and the short-circuit current i_{Rsc}. The slightly larger deviations of the torque for the higher speed of $n = 500$ r/min is mainly attributed to additional mechanical vibrations on the test stand, which become even more pronounced with increasing speed. The torque sensor has a limited stiffness, which, in combination with the test and load motor, results in a weakly damped spring-damper system with a resonance frequency at approximately $n = 600$ r/min. Therefore, no torque measurement results are included for $n = 750$ r/min and $n = 1000$ r/min in Fig. 9.

Note that for $n = 1000$ r/min the short-circuit current reaches almost 4 times the rated current of the machine. This value also corresponds to the maximum current allowed for the considered PMSM. Thus, experiments with higher speeds are not possible without damage of the motor. Moreover, large currents also cause a significant heating of the coils. Consequently, this heating results in an increase of the electrical resistance and slightly smaller measured currents i_{Rsc} compared to the currents predicted by the model for higher speeds of the PMSM.

V. Conclusion and Outlook

A systematic modeling framework for electric machines based on MECs was proposed in this article. It extends earlier results in [23] by a systematic inclusion of the electric interconnection of the motor coils with other electric components, as, e.g., the cabling or the inverter. The main motivation for the proposed modeling approach is to obtain a model with a small complexity, which serves as a basis for fast dynamic simulations and for a model-based controller and observer design. The proposed model is able to accurately describe an electric machine in its entire operating range, including operating ranges with significant magnetic saturation and nonfundamental wave characteristics.

The feasibility of the proposed modeling framework was demonstrated by applying the method to the modeling of a PMSM. It was shown that the calibrated model exhibits a high accuracy in the overall operating range of the PMSM, including the failure case of a winding short circuit. The resulting model is real-time capable, which is a prerequisite for the design of optimal nonlinear control strategies or fault detection algorithms, [29]. This modeling framework was also successfully applied to a dual three-phase PMSM with a short circuit between two terminals in [30]. A similar model accuracy could be obtained as in this work. In general, the proposed framework provides a systematic modeling tool for a wide range of electric motor (real-time) applications with different fault scenarios.

Current work of the authors deals with the application of the approach described in this article in a model-predictive control strategy. First simulation results show a high potential to improve the torque control accuracy both for the healthy and the fault case in comparison to the state of the art. Furthermore, the use of the model in fault detection and isolation strategies, in particular for multi-phase PMSMs, is a current field of research. Finally, it is worth noting that the proposed modeling framework can be extended to consider temperature effects that result from a heating of the coils or permanent magnets. A possible way to do this is by augmenting the MEC model by a thermal model, e.g., in the form of a lumped thermal network. Current research of the authors is also directed in the combination of such a thermal network model with the proposed MEC model.

Acknowledgment

The authors would like to thank M. Manderla for the helpful discussions.

References

[1] P. P. Florin, R. Mircea, P. Adrian-Cornel, R. Martis, and C. Martis, "Comparative analysis for an electric power steering system," in *Proc. 13th Int. Conf. Elect. Mach.*, Alexandroupoli, Greece, 2018, pp. 590–596.
[2] R. Menon, A. H. Kadam, N. A. Azeez, and S. S. Williamson, "A comprehensive survey on permanent magnet synchronous motor drive systems

for electric transportation applications," in *Proc. 42nd Annu. Conf. IEEE Ind. Electron. Soc.*, Florence, Italy, 2016, pp. 6627–6632.
[3] M. Zafarani, E. Bostanci, Y. Qi, T. Goktas, and B. Akin, "Interturn short-circuit faults in permanent magnet synchronous machines: An extended review and comprehensive analysis," *IEEE Trans. Emerg. Sel. Topics Power Electron.*, vol. 6, no. 4, pp. 2173–2191, Dec. 2018.
[4] S. Grubic, J. M. Aller, B. Lu, and T. G. Habetler, "A survey on testing and monitoring methods for stator insulation systems of low-voltage induction machines focusing on turn insulation problems," *IEEE Trans. Ind. Electron.*, vol. 55, no. 12, pp. 4127–4136, Dec. 2008.
[5] P. Arumugam, T. Hamiti, and C. Gerada, "Modeling of different winding configurations for fault-tolerant permanent magnet machines to restrain interturn short-circuit current," *IEEE Trans. Energy Convers.*, vol. 27, no. 2, pp. 351–361, Jun. 2012.
[6] L. Belguerras, J. Arellano-Padilla, P. Arumugam, T. Hamiti, S. Mezani, and C. Gerada, "Non-linear circuit based model of permanent magnet synchronous machine under inter-turn fault: A simple approach based on healthy machine data," *IET Elect. Power Appl.*, vol. 10, no. 6, pp. 560–570, 2016.
[7] H. Qian, H. Guo, and X. Ding, "Modeling and analysis of interturn short fault in permanent magnet synchronous motors with multistrands windings," *IEEE Trans. Power Electron.*, vol. 31, no. 3, pp. 2496–2509, Mar. 2016.
[8] Y. Qi, E. Bostanci, V. Gurusamy, and B. Akin, "A comprehensive analysis of short-circuit current behavior in PMSM interturn short-circuit faults," *IEEE Trans. Power Electron.*, vol. 33, no. 12, pp. 10784–10793, Dec. 2018.
[9] Z. Sun, J. Wang, D. Howe, and G. Jewell, "Analytical prediction of the short-circuit current in fault-tolerant permanent-magnet machines," *IEEE Trans. Ind. Electron.*, vol. 55, no. 12, pp. 4210–4217, Dec. 2008.
[10] B. Sen and J. Wang, "Stator interturn fault detection in permanent-magnet machines using PWM ripple current measurement," *IEEE Trans. Ind. Electron.*, vol. 63, no. 5, pp. 3148–3157, May 2016.
[11] J. Härsjö and M. Bongiorno, "Modeling and harmonic analysis of a permanent magnet synchronous machine with turn-to-turn fault," in *Proc. 17th Eur. Conf. Power Electron. Appl., EPE-ECCE Eur.*, Geneva, Switzerland, 2015, pp. 1–10.
[12] M. A. Mazzoletti, G. R. Bossio, C. H. D. Angelo, and D. R. Espinoza-Trejo, "A model-based strategy for interturn short-circuit fault diagnosis in PMSM," *IEEE Trans. Ind. Electron.*, vol. 64, no. 9, pp. 7218–7228, Sep. 2017.
[13] O. Dieterle, T. Greiner, and P. Heidrich, "Control of a PMSM with quadruple three-phase star-connected windings under inverter short-circuit fault," *IEEE Trans. Ind. Electron.*, vol. 66, no. 1, pp. 685–695, Jan. 2019.
[14] B.-G. Gu, J.-H. Choi, and I.-S. Jung, "Development and analysis of interturn short fault model of PMSMs with series and parallel winding connections," *IEEE Trans. Power Electron.*, vol. 29, no. 4, pp. 2016–2026, Apr. 2014.
[15] W. Wang, J. Zhang, M. Cheng, and S. Li, "Fault-tolerant control of dual three-phase permanent-magnet synchronous machine drives under open-phase faults," *IEEE Trans. Power Electron.*, vol. 32, no. 3, pp. 2052–2063, Mar. 2017.
[16] P. C. Krause, O. Wasynczuk, and S. D. Sudhoff, *Analysis of Electric Machinery and Drive Systems*. Piscataway, NJ, USA: IEEE Press, 2002.
[17] J. Chiasson, *Modeling and High-Performance Control of Electric Machines*. Hoboken, NJ, USA: Wiley, 2005.
[18] G. Choi and T. M. Jahns, "PM synchronous machine drive response to asymmetrical short-circuit faults," *IEEE Trans. Ind. Electron.*, vol. 52, no. 3, pp. 2176–2185, May/Jun. 2016.
[19] M. Fitouri, Y. Bensalem, and M. N. Abdelkrim, "Modeling and detection of the short-circuit fault in PMSM using finite element analysis," *IFAC-PapersOnLine*, vol. 49, no. 12, pp. 1418–1423, 2016.
[20] V. Ostovic, *Dynamics of Saturated Electric Machines*. New York, NY, USA: Springer, 1989.
[21] P. Naderi, "Magnetic-equivalent-circuit approach for inter-turn and demagnetisation faults analysis in surface mounted permanent-magnet synchronous machines using pole specific search-coil technique," *IET Electric Power Appl.*, vol. 12, no. 7, pp. 916–928, 2018.
[22] D. Faustner, W. Kemmetmüller, and A. Kugi, "Magnetic equivalent circuit modeling of a saturated surface-mounted permanent magnet synchronous machine," *IFAC-PapersOnLine*, vol. 48, no. 1, pp. 360–365, 2015.
[23] W. Kemmetmüller, D. Faustner, and A. Kugi, "Modeling of a permanent magnet synchronous machine with internal magnets using magnetic equivalent circuits," *IEEE Trans. Magn.*, vol. 50, no. 6, Jun. 2014, Art. no. 8101314.
[24] N. Christofides, *Graph Theory: An Algorithmic Approach*. New York, NY, USA: Academic, 1975.
[25] A. Kugi, *Non-linear Control Based on Physical Models*. London, U.K.: Springer, 2001.
[26] D. Hanselman, *Brushless Permanent Magnet Motor Design*, 2nd ed., Orono, ME, USA: The Writers' Collective, 2003.
[27] L. T. Biegler, *Nonlinear Programming: Concepts, Algorithms, and Applications to Chemical Processes*. Philadelphia, PA, USA: Society for Industrial and Applied Mathematics, 2010.
[28] D. G. Luenberger and Y. Ye, *Linear and Nonlinear Programming*. Basel, Switzerland: Springer, 2016.
[29] W. Kemmetmüller, D. Faustner, and A. Kugi, "Optimal torque control of permanent magnet synchronous machines using magnetic equivalent circuits," *Mechatronics*, vol. 32, no. 1, pp. 22–33, 2015.
[30] G. Forstner, A. Kugi, and W. Kemmetmüller, "Magnetic equivalent circuit model of a dual three-phase PMSM with winding short circuit," in *Proc. 45th Annu. Conf. IEEE Ind. Electron. Soc.*, Lisbon, Portugal, 2019, pp. 1177–1182.

Gabriel Forstner (Student Member, IEEE) received the Dipl.-Ing. degree in information technology from the University Klagenfurt, Klagenfurt, Austria, in 2015. He is currently working toward the Ph.D. degree in control engineering with the Automation and Control Institute (ACIN), TU Wien, Vienna, Austria.

His main research interests include the physics based modeling and the optimal control of mechatronic systems with a focus on permanent magnet synchronous motors.

Andreas Kugi (Senior Member, IEEE) received the Dipl.-Ing. degree in electrical engineering from Graz University of Technology, Graz, Austria, in 1992, the Ph.D. degree in control engineering and the Habilitation degree in automatic control and control theory from Johannes Kepler University (JKU), Linz, Austria, in 1995 and 2000, respectively.

He was an Associate Professor with Johannes Kepler University Linz, from 2000 to 2002. He was a Full Professor with Saarland University, Saarbrücken, Germany, from 2002 to 2007. Since 2007, he has been the Head of the Automation and Control Institute (ACIN), TU Wien, Vienna, Austria, and since 2017, he has also been the Head of the Center for Vision, Automation and Control, Austrian Institute of Technology (AIT). His main research interests include the modeling, control and optimization of complex dynamical systems, the mechatronic system design as well as robotics and process automation.

Dr. Kugi is Full Member of the Austrian Academy of Sciences and member of the German National Academy of Science and Engineering (Acatech).

Wolfgang Kemmetmüller (Member, IEEE) received the Dipl.-Ing. degree in mechatronics from the Johannes Kepler University Linz, Linz, Austria, in 2002, the Ph.D. degree in control engineering from Saarland University, Saarbruecken, Germany, in 2007, and the Habilitation degree in system theory and automatic control from TU Wien, Vienna, Austria, in 2016.

He is currently an Associate Professor with the Automation and Control Institute, TU Wien. His research interests include the physics based modeling and the nonlinear control of mechatronic systems with a special focus on power electronics, electrohydraulic, and electromechanical systems.